A Long Time Ago in a Galaxy Far, Far Away:
A Candidate $z \sim 14$ Galaxy in Early *JWST* CEERS Imaging

Steven L. Finkelstein, Micaela B. Bagley, Pablo Arrabal Haro, Mark Dickinson, Henry C. Ferguson,
Jeyhan S. Kartaltepe, Casey Papovich, Denis Burgarella, Dale D. Kocevski, Marc Huertas-Company,
Kartheik G. Iyer, Anton M. Koekemoer, Rebecca L. Larson, Pablo G. Pérez-González, Caitlin Rose,
Sandro Tacchella, Stephen M. Wilkins, Katherine Chworowsky, Aubrey Medrano, Alexa M. Morales,
Rachel S. Somerville, L. Y. Aaron Yung, Adriano Fontana, Mauro Giavalisco, Andrea Grazian,
Norman A. Grogin, Lisa J. Kewley, Allison Kirkpatrick, Peter Kurczynski, Jennifer M. Lotz,
Laura Pentericci, Nor Pirzkal, Swara Ravindranath, Russell E. Ryan Jr., Jonathan R. Trump, Guang Yang,

AND The CEERS Team:

Omar Almaini, Ricardo O. Amorín, Marianna Annunziatella, Bren E. Backhaus, Guillermo Barro,
Peter Behroozi, Eric F. Bell, Rachana Bhatawdekar, Laura Bisigello, Volker Bromm, Véronique Buat,
Fernando Buitrago, Antonello Calabrò, Caitlin M. Casey, Marco Castellano, Óscar A. Chávez Ortiz,
Laure Ciesla, Nikko J. Cleri, Seth H. Cohen, Justin W. Cole, Kevin C. Cooke, M. C. Cooper,
Asantha R. Cooray, Luca Costantin, Isabella G. Cox, Darren Croton, Emanuele Daddi, Romeel Davé,
Alexander de la Vega, Avishai Dekel, David Elbaz, Vicente Estrada-Carpenter, Sandra M. Faber,
Vital Fernández, Keely D. Finkelstein, Jonathan Freundlich, Seiji Fujimoto, Ángela García-Argumánez,
Jonathan P. Gardner, Eric Gawiser, Carlos Gómez-Guijarro, Yuchen Guo, Kurt Hamblin,
Timothy S. Hamilton, Nimish P. Hathi, Benne W. Holwerda, Michaela Hirschmann, Taylor A. Hutchison,
Saurabh W. Jha, Shardha Jogee, Stéphanie Juneau, Intae Jung, Susan A. Kassin, Aurélien Le Bail,
Gene C. K. Leung, Ray A. Lucas, Benjamin Magnelli, Kameswara Bharadwaj Mantha, Jasleen Matharu,
Elizabeth J. McGrath, Daniel H. McIntosh, Emiliano Merlin, Bahram Mobasher, Jeffrey A. Newman,
David C. Nicholls, Viraj Pandya, Marc Rafelski, Kaila Ronayne, Paola Santini, Lise-Marie Seillé,
Ekta A. Shah, Lu Shen, Raymond C. Simons, Gregory F. Snyder, Elizabeth R. Stanway, Amber N. Straughn,
Harry I. Teplitz, Brittany N. Vanderhoof, Jesús Vega-Ferrero, Weichen Wang, Benjamin J. Weiner,
Christopher N. A. Willmer, Stijn Wuyts And Jorge A. Zavala

ABSTRACT

We report the discovery of a candidate galaxy with a photo-z of $z \sim 14$ in the first epoch of the *JWST* Cosmic Evolution Early Release Science (CEERS) Survey. Following conservative selection criteria we identify a robust source at $z_{phot} = 14.3^{+0.4}_{-1.1}$ (1σ uncertainty) with $m_{F277W} = 27.8$, and $>5\sigma$ detections in five filters. This object (Maisie's Galaxy) exhibits F150W−F200W>2.5 mag with a blue continuum slope, resulting in 99.99% (87%) of the photo-z PDF favoring $z > 10$ (13). All data quality images show no artifacts at the candidate's position, and independent analyses consistently find a strong preference for $z > 13$. The source may be marginally detected in *HST* F160W, which if included would widen the lower-redshift bound to $z \sim 12.5$, and would require very strong Lyα emission ($\gtrsim 300$Å rest-EW) indicating an early ionized bubble. Its colors are inconsistent with Galactic stars, and it is resolved ($r_h = 330 +/- 30$ pc). Maisie's Galaxy appears modestly massive (log $M_*/M_\odot \sim$ 8.5) and highly star-forming (log sSFR~ -7.9 yr^{-1}), with a blue rest-UV color ($\beta \sim -2.3$) indicating little dust though not extremely low metallicities. While the presence of this source is in tension with most predictions, it agrees with empirical extrapolations assuming a smoothly declining SFR density. Should followup spectroscopy validate this redshift, our Universe was already aglow with galaxies less than 300 Myr after the Big Bang.

Keywords: Early universe (435); Galaxy formation (595); Galaxy evolution (594); High-redshift galaxies (734)

1. INTRODUCTION

stevenf@astro.as.utexas.edu

The study of galaxy evolution is the ultimate human origin story – not just how did our species, planet or Solar System come to be, but this field seeks to answer how our Milky Way Galaxy came to be. One method to study our Galactic origins is to study the earliest build-

ing blocks of the Milky Way by searching for and analyzing galaxies forming in the early Universe. The advent of the Wide Field Camera 3 (WFC3) on the *Hubble Space Telescope* (*HST*) pushed our cosmic horizons well into the epoch of reionization, the time when energetic photons (presumably from massive stars in early galaxies) ionized the gas in the intergalactic medium (IGM; e.g. Finkelstein 2016; Stark 2016; Robertson 2021, and references therein). These studies found that the $z = 6$–10 universe is teeming with galaxies, with thousands of galaxy candidates known, including spectroscopic confirmations out to $z \sim 11$ (Oesch et al. 2016; Jiang et al. 2021).

One key focus in these studies has been the evolution of the cosmic star-formation rate density (SFRD). This quantity is well known to rise from the present day to the peak of cosmic star-formation at $z \sim 2$–3, then declining again to early times (e.g. Madau & Dickinson 2014). As the aforementioned WFC3 studies pushed to higher redshifts, it became of interest to study whether the cosmic SFRD, which exhibited a smooth decline from $z = 4$–8 (e.g. Bouwens et al. 2015; Finkelstein et al. 2015), continued to decline smoothly to even higher redshifts. Results in the literature were mixed, with some studies finding evidence for an accelerated decline in the SFRD (e.g. Oesch et al. 2018; Bouwens et al. 2021), while others found that observations supported a continued smooth decline (e.g. Coe et al. 2013; McLeod et al. 2016; Finkelstein & Bagley 2022). Simulations do make predictions for the evolution of the SFRD, but these predictions span a wide range (e.g. Gnedin 2016; Dayal & Ferrara 2018; Tacchella et al. 2018; Yung et al. 2019; Behroozi et al. 2020).

Part of the difficulty of such studies is the near-heroic observational effort needed to study galaxies at $z \sim 10$ with *HST*. These galaxies become more and more difficult to see with this 2.4m ultraviolet (UV)/optical/near-IR telescope, and at these high-redshifts they become single-band detections, leaving the $z \gtrsim 11$ universe opaque to our understanding. To avoid being dominated by spurious sources, studies employ a variety of vetting criteria to ensure robust samples of candidate galaxies (e.g. Bouwens et al. 2021; Bagley et al. 2022; Finkelstein et al. 2022), which makes it difficult to estimate the sample completeness and thereby to obtain a robust estimate of the SFRD.

This all changes with the advent of the *James Webb Space Telescope* (*JWST*). The dramatic increase in light-gathering power coupled with the infrared sensitivity makes this telescope the ideal machine to push our cosmic horizons to the epoch of the first galaxies. As the first *JWST* images arrive it is natural to wonder what these early data tell us about the rise of star-formation in the early universe. If the SFRD really declines as steeply at $z > 8$ as has been proposed, few galaxies at $z > 11$ should be detectable in early *JWST* data. If the decline is instead more gradual one might expect to discover galaxies at $z \sim 12$ or even higher. In just the first week since the data have been released exciting results already indicate significant star formation is occurring at $z > 11$ (e.g. Castellano et al. 2022; Naidu et al. 2022).

As another early probe of this epoch, here we report on a search for the highest redshift ($z = 12$–15) galaxies in the first epoch of imaging from the Cosmic Evolution Early Release Science Survey (CEERS; Finkelstein et al. in prep). These data were among the first Cycle 1 science exposures taken, and were included in the first publicly released data on July 14. §2 describes the observations and data reduction, while §3 describes our photometry, photometric redshift measurement, and sample selection procedure. §4 presents our results, and we discuss these results in §5. Our conclusions are presented in §6. In this paper we assume the latest *Planck* flat ΛCDM cosmology with H_0 =67.36, Ω_m =0.3153, and Ω_Λ =0.6847 (Planck Collaboration et al. 2020). All magnitudes are in the absolute bolometric system (AB Oke & Gunn 1983).

2. OBSERVATIONS

2.1. *CEERS Data*

CEERS is one of 13 early release science surveys designed to obtain data covering all areas of astronomy early in Cycle 1. CEERS is based around a mosaic of 10 NIRCam pointings, with six obtaining NIRSpec in parallel, and four with MIRI in parallel (four of these pointings also include NIRCam wide-field slitless grism spectroscopy). Here we make use of the first four CEERS NIRCam pointings, obtained on 21 June 2022, known as CEERS1, CEERS2, CEERS3, and CEERS6.

In each pointing, data were obtained in the short-wavelength (SW) channel F115W, F150W, and F200W filters, and long-wavelength (LW) channel F277W, F356W, F410M, and F444W filters. The total exposure time for pixels observed in all three dithers was typically 2835 s per filter. The exception is F115W, which obtained double the exposure time to increase the depth on the filter covering the wavelength range below the Lyman-α break at $z > 10$. The full details on the readout and dither patterns will be available in the CEERS overview paper (Finkelstein et al. in prep).

2.2. *Data Reduction*

We performed a careful initial reduction of the NIRCam images in all four pointings, using version 1.5.3

of the *JWST* Calibration Pipeline[1] with some custom modifications. We used the current (15 July 2022) set of NIRCam reference files[2], though we note that the majority were created pre-flight, including the flats and photometric calibration references. We describe our reduction steps below, and present more details in Bagley et al. (in prep).

Beginning with the raw data, we used Stage 1 of the pipeline with all default parameters to apply detector-level corrections, fit the ramps in each integration, and output countrate maps. We next performed a custom step to remove *1/f* noise, which is correlated noise introduced in the images during the detector readout that presents as horizontal and vertical striping patterns (Schlawin et al. 2020). We applied the flat field to the countrate maps to ensure we were measuring the *1/f* noise pattern on a flat image. We then masked all bad pixels and source flux, using PHOTUTILS (Bradley et al. 2020) to detect sources and dilating the resulting segmentation map by 21 pixels. First for each row and then each column, we measured a sigma-clipped median value and subtracted this value from the un-flat-fielded countrate map. In the SW channel images, this correction was performed amplifier-by-amplifier. However, we measured the median across each full row in the LW images, as an amplifier-dependent correction would be biased by the significant residual flat field structure present in the LW images due to our use of ground flat reference files.

After processing the cleaned countrate maps through Stage 2 of the pipeline, we performed an astrometric calibration using an edited version of the TweakReg step of the pipeline. The TweakReg step detects sources in each input image, identifies their counterparts in the reference catalog, and calculates a rotation and a shift in x and y to correct the image WCS. In lieu of using the default options that allow for alignment to Gaia DR2, we used a reference catalog derived from a *HST* F160W 0.03″/pixel mosaic[3] in the EGS field with astrometry tied to Gaia-EDR3 (see Koekemoer et al. 2011, for details). We found that due to initial WCS offsets between detectors, we had to align exposures in separate groups. We fit module A and B separately for the LW images, and fit the SW images in three sets: (1) all module A detectors, (2) detector B2, and (3) the remaining three detectors of module B. We first aligned F200W to the F160W reference catalog, and then used

PHOTUTILS to create a new reference catalog in F200W, which we used to align all other NIRCam filters. We cleaned the F200W reference catalog of all sources near detector edges and spurious sources around diffraction spikes and in the noise around bright sources, and considered only compact sources in the magnitude range $18 < m_{200} < 27$.

We fit and removed a single value in MJy/sr from each calibrated detector image separately before coadding the images onto a common output grid. The coadding was performed using the drizzle algorithm with an inverse variance map weighting (Fruchter & Hook 2002; Casertano et al. 2000) via the Resample step in the pipeline. The output mosaics have pixels scales of 0″03/pixel. The median astrometric offset in each filter and NIRCam pointing is $\lesssim 0.005″$, and the RMS is $\sim 0.025″ - 0.03″$ (~ 1 pixel). In one detector of one NIRCam pointing (CEERS1), there were not enough compact sources with significant signal-to-noise to find a satisfactory WCS solution. As a result, the alignment in this region is off by several pixels, and so we have masked this region ($\sim 1/32$ of the total area) in our analysis. Additionally, the pipeline-produced ERR maps contain a bug resulting in low-rms holes, and so we made effective rms maps as the inverse square root of the weight maps. The usable total area covered by these observations, calculated from the number of pixels with low effective error-map values in all of the F115W, F150W, F200W, F277W, and the detection image (see below) is 34.5 arcmin^2.

We note that our data reduction represents a preliminary version, with several aspects that will be improved with the release of updated NIRCam reference files. We also have not removed the features known as "wisps" and "snowballs" from the mosaics at this time. However, the wisp features are removed during our background subtraction (see Section 3.1). Additionally, we have carefully inspected all input exposures to ensure that the fluxes in all filters are unaffected by snowballs (see Section 4.2).

3. METHODOLOGY

3.1. *Photometric Catalog Construction*

The full details of our photometric analysis will be presented in Finkelstein et al. (2022d, in prep; hereafter F22d); here we briefly summarize our procedures (many of which are similar to Finkelstein et al. 2022). The data products from our modified data reduction pipeline come in the form of multi-extension "i2d" files. We first estimate and subtract any residual background using a custom Python-based algorithm. This routine iteratively convolves the image with Gaussian kernels of progressively smaller sizes, then uses PHOTUTILS to

[1] jwst-pipeline.readthedocs.io

[2] jwst-crds.stsci.edu, jwst_nircam_0214.imap

[3] ceers.github.io/hdr1.html

mask pixels identified with sources in four iterations to mask progressively smaller sources, dilating the masks in between iterations, then measuring the background after masking with PHOTUTILS.BACKGROUND2D.

The i2d file was split into separate extensions, subtracting this background from the SCI extension. Empirical PSFs were made by stacking stars, and the F115W, F150W, F200W, and F277W images were PSF-matched to the F356W image using PYPHER. Photometry was computed on the PSF-matched images using SOURCE EXTRACTOR (hereafter SE; Bertin & Arnouts 1996) v2.25.0 in two image mode, with an inverse-variance weighted combination of the PSF-matched F277W and F356W images as the detection image, with photometry measured on all seven bands.

Colors were measured in small Kron apertures with a Kron factor of 0.8 and a Kron minimum radius of 1.1; this is smaller than previous studies, which we found necessary to keep the elliptical aperture close to the significant isophotes of small, faint galaxies. An aperture correction was derived in the F356W catalog as the ratio between the flux measured in the default Kron aperture (with PHOT_AUTOPARAMS 2.5, 3.5) to that in our small Kron aperture. This correction was applied to all fluxes and uncertainties. We use the CEERS simulated imaging[4] to test the accuracy of this procedure, finding that after this aperture correction, total fluxes were underestimated by ∼10-15%, rising to 22% in F444W (understandable due to the larger point-spread function [PSF] in F444W as the photometric apertures were defined on F356W). We apply these simulation-based corrections (comparable to similar corrections applied in *HST* studies; Finkelstein et al. e.g. 2022) to all fluxes and uncertainties to complete our total flux measurements. All fluxes and uncertainties were corrected for Galactic attenuation assuming a field-averaged E(B-V)=0.006 and a Cardelli et al. (1989) Milky Way attenuation curve. We also measure fluxes in a range of circular apertures; as these are used for detection significance tests, we do not correct them to total fluxes (though they are still corrected for Galactic attenuation).

The pipeline error and weight maps do not presently have the correct scaling; thus we derive flux uncertainties directly from the data, following Finkelstein et al. (2022), based on previous methodology outlined in Papovich et al. (2016). We fit for the noise as a function of aperture size by measuring the fluxes at $\sim5\times10^3$ randomly-placed positions in 15 circular apertures with

diameters ranging from 1 – 100 pixels, fitting a polynomial function to the standard deviation in aperture fluxes as a function of the number of pixels in each aperture. We then use this function to calculate the photometric uncertainties for each object for a given aperture area. These values were scaled by the ratio of the error image value at the central position of a given source to the median error value of the whole map. All aperture and Galactic attenuation corrections were applied to these uncertainties. Finally, around each source in our catalog, we calculate a "local" noise estimate, as the standard deviation in flux values from these previously placed random apertures within a 300 pixel radius of a source (increasing the radius when necessary to reach a minimum of 50 apertures).

The NIRCam photometric zero points used for the data reduction are based on pre-flight measurements. The throughputs of NIRCam are reported to be close to or higher than the pre-flight measurements (Rigby et al. 2022, see their Figure 8). To validate our photometry, we fit stellar-population models to ∼4000 spectroscopically-selected galaxies in CANDELS and used those models to predict the NIRCam fluxes in all of the bands. The predicted fluxes agree to within 2-5% (depending on the band) with the measured *JWST* photometry using the pre-flight zero points (see F22d for more details on this test).

3.2. *Photometric Redshifts*

We use the EAZY (Brammer et al. 2008) software package to estimate photometric redshifts for all sources in our photometric catalog. EAZY fits non-negative linear combinations of user-supplied templates to derive probability distribution functions (PDFs) for the redshift, based on the quality of fit of the various template combinations to the observed photometry for a given source. The template set we use includes the "tweak_fsps_QSF_12_v3" set of 12 templates recommended by the EAZY documentation. To this we add a set of six additional templates spanning bluer colors than the FSPS models, as Larson et al. (2022, in prep) found that these improve the accuracy of photometric redshift fits for the expected blue colors of $z > 9$ galaxies. We do not use the luminosity prior (e.g., a flat prior is assumed) as the epoch in question is completely unexplored. Our fiducial EAZY run uses our Kron-aperture measured colors. We also perform two ancillary runs which we use for later vetting. One uses fluxes measured in $0.3''$ circular apertures (to cover the possibility that a Kron ellipse was drawn inaccurately, which happens in the presence of bright neighbors). A second run had a

---

[4] Simulated Data Release 3; ceers.github.io/sdr3.html

maximum redshift of $z = 7$ to allow the exploration of secondary redshift solutions.

3.3. Sample Selection

To select our sample of candidate very high redshift galaxies, we follow previous work done by our team (Finkelstein et al. 2015; Rojas-Ruiz et al. 2020; Finkelstein et al. 2022; Bagley et al. 2022). We make use of both photometric signal-to-noise criteria, to ensure robust photometric detections (to minimize the chance of a spurious signal), and ensure robust non-detections below the Lyman-α break. We add to these several criteria based off of the full EAZY redshift PDF (denoted $\mathcal{P}(z)$). We note that the criteria imposed here are fairly conservative - we wish to identify the most robust highest-redshift candidates. Future work will explore how to relax some of these criteria to improve sample completeness, without introducing unacceptable levels of contamination.

To derive an initial sample of $z > 12$ galaxies, we first impose all following requirements:

- Signal-to-noise (SNR) in both F200W and F277W > 6 in conservatively small $0.2''$ (6.7-pixel) diameter apertures for these measurements, using both the fiducial (global) and local noise estimates.

- Error map values < 1000 (indicating coverage by the majority of exposures) in F115W, F150W, F200W, F277W and the detection image.

- Initial more inclusive photometric redshift cuts of $\int \mathcal{P}(z > 8) \geq 0.9$, $z_{best} > 8.5$, $\chi^2_{EAZY} < 20$ (to reject poor EAZY fits), and that the $\Delta z = 1$ integer redshift bin (z_{sample}) with the largest integrated $\mathcal{P}(z)$ to be at $z_{sample} \geq 9$.

- Objects at $z_{sample} > 10$ must have SNR ≤ 2.0 in F115W, while objects at $z_{sample} > 13$ must have a SNR ≤ 2.0 in both F115W and F150W (in both the global and local noise in $0.2''$-diameter apertures). These redshifts correspond to the wavelength of the Lyman-α break leaving a given dropout filter.

- F200W magnitude < 29, to focus on well-detected objects regardless of formal SNR.

After this initial set of selection criteria, we examined the resulting objects. We inspected their spectral-energy distributions (SEDs), image stamps, and $\mathcal{P}(z)$ plots. We noticed several low-confidence sources which could be identified with further automated cuts. We thus implemented this additional set of selection criteria:

- We additionally implement all of the above detection significance criteria, both in the detection and dropout bands, in a $0.3''$-diameter aperture to account for situations where faint flux was visible slightly off-center of the source barycenter (especially important given the astrometric scatter discussed in §2).

- We require the χ^2 from an additional EAZY run with a maximum redshift of seven to have a significantly worse fit than our fiducial run via $\chi^2_{Low-z} - \chi^2_{fiducial} > 4$.

- We impose a single color cut of F200W - F444W < 1 to reduce the incidence of red low-redshift interlopers. This is similar to the color cuts simulated by Hainline et al. (2020) and implemented by Castellano et al. (2022).

- To account for situations where the Kron aperture could be affected by nearby bright sources, we also require $\int \mathcal{P}(z > 8) \geq 0.5$ from an independent EAZY run performed with colors measured in $0.3''$ circular apertures.

- We require the integrated $\mathcal{P}(z)$ at $12 < z < 15$ to be higher than that at $8.5 < z < 10$ or $10 < z < 12$, to hone in on the highest-redshift galaxies.

Running the above selection process on all four fields, we initially find 12 $z > 12$ galaxy candidates. We perform an initial visual inspection of these candidates, inspecting $1.5''$ image stamps in all filters, and $5''$ image cutouts in F200W and the detection image. We find three objects are obvious artifacts; one due to an image edge, and two due to cosmic-ray residual "snowballs". After removal of these three, this initial sample consistent of nine candidate $z > 12$ galaxies, 1, 5, 1 and 2 in the CEERS1, CEERS2, CEERS3 and CEERS6 pointings, respectively.

Of these nine candidates, we noticed that multiple sources exhibited SNR > 1.5 in either F115W or F150W. As our goal is a conservatively robust sample of extreme-redshift sources, we elect to further remove sources with SNR $= 1.5$–2 in either of F115W or F150W in our fiducial $0.2''$-diameter apertures, leaving five sources. However, these flux levels are only of marginal significance, and could easily be due to image noise or even faint line-of-sight interlopers. We explore this by estimating the probability that flux at the 1-2 σ level, from statistical fluctuations or low-surface brightness intervening sources, is detected in the dropout bands of high-redshift galaxies. We did this by placing at random in the dropout image 5×10^4 photometric apertures

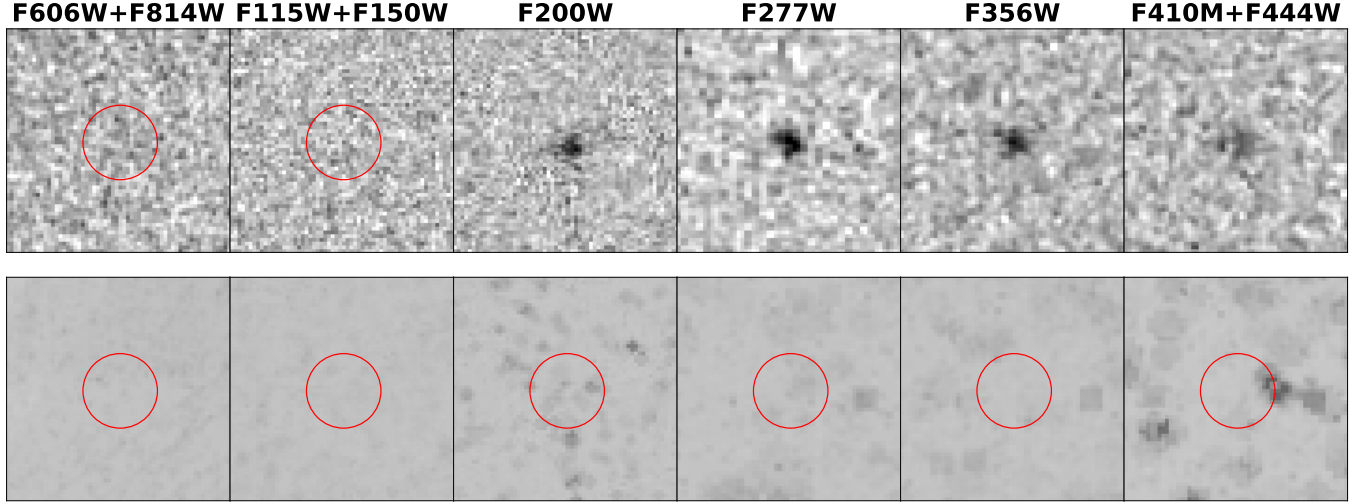| F606W+F814W	F115W+F150W	F200W	F277W	F356W	F410M+F444W

Figure 1. Top) $1.8'' \times 1.8''$ cutout images centered on the position of Maisie's Galaxy in the non-PSF-matched images. This source exhibits the hallmark colors of a distant galaxy – no discernible flux in a dropout band (we show stacked F606W+F814W and F115W+F150W images; the circle has a radius of $0.3''$) and a significant detection in the bluest detection band (F200W in this case). The wide wavelength range of NIRCam allows this source to be well-detected in multiple filters, and in the imaging alone it is clear this source exhibits a blue spectral shape. Bottom) Same ordering as the top, for sky-uncertainty maps constructed from the variance of the readout noise, all using a linear scale from 0.33 to $3\times$ the robustly-measured sky standard deviation in each band. The patchiness of the uncertainties is due to loss of exposure time when cosmic-rays are detected and rejected in the multiple readouts or in outlier rejection when combining the dithered exposures (the $2\times$ larger original pixel scale of the long-wavelength channels results in larger patches than the short-wavelength channels). The uncertainty arrays show no excess in rejected pixels near the candidate galaxy.

of the same size as those used for the candidates and count the number of detections at a given SNR level. We found that SNR=1.5-significance flux was detected 25.1% (26.4%) of the time in F115W (F150W), and SNR=2-significance flux was detected 24.1% (25.0%). This implies that many of the candidates removed due to our strict dropout SNR criteria (including those listed in the Appendix) may be genuine high-redshift sources.

As a final vetting step, we measure fluxes at the positions of the remaining five candidate galaxies in the CANDELS ACS (e.g., Grogin et al. 2011; Koekemoer et al. 2011) imaging, using the new v1.9 images released by the CEERS team (updating astrometry to GAIA). As our NIRCam images were not on the same pixel grid as the ACS images, we measure forced photometry in $0.2''$-diameter apertures using the methodology outlined in §4.1 of Finkelstein et al. (2022). We find that three sources have SNR >1.5 in at least one *HST* ACS image (details are in the appendix table), thus following our conservative dropout criteria, we remove these three sources from our sample.

After the above process, our sample included two candidate $z > 12$ galaxies. Of these two candidates, one appears robustly detected with SNR > 10 in several filters, while the other only just satisfied our detection

Table 1. Properties of Maisie's Galaxy

Property	Value
Source ID	CEERSJ141946.35+525632.8
RA (J2000 [deg])	214.943153
Dec (J2000 [deg])	52.942449
z_{EAZY}	$14.3^{+0.4}_{-1.1}$
$\mathcal{T}_{BigBang}$	286^{+36}_{-10} Myr
M_{UV} (mag)	$-20.3^{+0.1}_{-0.1}$
β	$-2.32^{+0.11}_{-0.20}$
log (M*/M$_\odot$)	$8.45^{+0.33}_{-0.32}$
A$_v$ (mag)	$0.06^{+0.23}_{-0.04}$
SFR$_{10Myr}$ (M$_\odot$ yr^{-1})	$4.1^{+4.2}_{-3.5}$
log sSFR$_{10Myr}$ (yr^{-1})	$-7.9^{+0.7}_{-0.9}$
Mass-weighted Age (Myr)	16^{+45}_{-6}

Note—$\mathcal{T}_{BigBang}$ is the time elapsed from the Big Bang to the photometric redshift for our assumed cosmology. The physical properties listed below the horizontal line were derived with Prospector.

significance criteria in two filters. We thus focus the remainder of this paper on the more robust source (the other object is ID 971 in the appendix table, and will be analyzed in future work).

4. RESULTS

4.1. *A Robust Galaxy Candidate at z = 14*

This source, CEERSJ141946.35+525632.8, hereafter known as "Maisie's Galaxy"[5] was detected in the CEERS2 field. Promisingly, it was first identified in the earliest (v0.02) internal CEERS reduction in this field, being the first $z \sim 14$ candidate viewed on 18 July, 2022. In each subsequent reduction, this source continued to satisfy all selection criteria, becoming progressively more robust as the data became cleaner. Several CEERS team members viewed all nine potential $z \sim 14$ candidates above on 22 July 2022, and agreed on the robustness of this source. The photometric redshift of this source is $z = 14.3^{+0.4}_{-1.1}$, which (for our assumed cosmology) corresponds to an age of the Universe of 286^{+36}_{-10} Myr. The properties of this galaxy are summarized in Table 1, and we list its photometry in Table 2.

Figure 1 shows cutouts of this candidate galaxy in the NIRCam bands, while Figure 2 shows two color composites. Figure 3 shows the observed spectral energy distribution of our candidate with photometric redshift fits. The confidence of this source as a robust very high-redshift galaxy is easy to see from all three of these figures. The Lyman-α break color, here F150W-F200W, is >2.5 mag (1σ), completely eliminating any known low-redshift interloper. Such a model would need to have an extremely red color to match our F150W-F200W >2.5 mag break, but then have a very blue color. While lower-redshift passive or dusty galaxies can mimic high-redshift Lyman-α breaks, the observed >2.5 mag break is much larger than known populations of low-redshift galaxies. Such galaxies would also be fairly red redward of the break. Though differential geometry could accommodate UV spectral slopes as blue as $\beta \sim -1$, this object has $\beta \sim -2.3$ (see §5.1; Casey et al. 2014). The significant detection in four broadband filters also rules out low-redshift extreme emission line galaxies. We show as the orange curve in Figure 3 EAZY's best-fitting low-redshift model, which is ruled out at high confidence. Based on the non-detection in F150W and strong detection in F200W, the implied redshift is $z > 13$. This is confirmed by the EAZY fit, shown as the blue line, which prefers $z \sim 14.3$ (due to the slightly red F200W-F277W, indicating the Lyα break is just inside the blue side of F200W).

---

[5] This exceptional source survived all detailed analysis steps, firmly becoming a plausible candidate on the ninth birthday of the lead author's daughter. We adopt this short name for convenience in this and future papers.
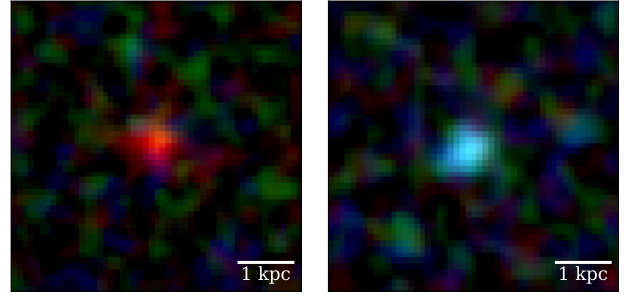

Figure 2. Three-color images of Maisie's Galaxy. The left image is a composite of *HST*/ACS F606W and F814W in blue, F115W and F150W in green, and F200W in red. This shows the galaxy candidate as red due to the very high redshift resulting in no detected flux in the filters assigned to the blue and green colors. The right image shows an approximated "true" rest-UV color image, composed entirely of the long-wavelength channel filters F277W in blue, F356W in green, F410M+F444W in red). As we discuss further in §4, intrinsically this galaxy is quite blue. The scale bar corresponds to 1 (physical) kpc assuming $z = 14$ at a scale of 0.3″ per kpc.

4.2. *Fidelity of Candidate*

Figure 1 shows 1.8″ cutout images of this source at multiple wavelengths. This source shows the expected pattern for a high-redshift galaxy, with no significant flux in mutliple dropout bands, with robust flux in redder bands. The very sharp break between F150W and F200W is consistent with a redshift of $z > 13$. The advantage of *JWST* is clear here, as this source is well-detected in all five NIRCam filters redward of the break. This multi-band detection essentially eliminates the possibility of a spurious nature. Of note is that while persistence from previous observations affected several *HST* programs (see discussion in Finkelstein et al. 2022 and Bagley et al. 2022), CEERS observed with the bluest filters first, thus any flux from persistence would be most apparent in F115W.

To further rule out a spurious nature, the science, error, and data-quality images were visually inspected at the position(s) of the best candidate(s). This is to ensure that the detected sources in the co-added images are not just chance super-positions of regions that were affected by cosmic rays or other artifacts. In the case of the $z \sim 14$ candidate, the source is visible in all of the individual F200W, F277W, and F356W exposures, and overlaps with a cosmic ray in only a few images. Even in those cases, the cosmic rays that are masked in the data-quality array are of the typical size that is cleanly rejected in the jump-detection step of the pipeline. There were no overlaps with the larger "snowball" charged-particle events.
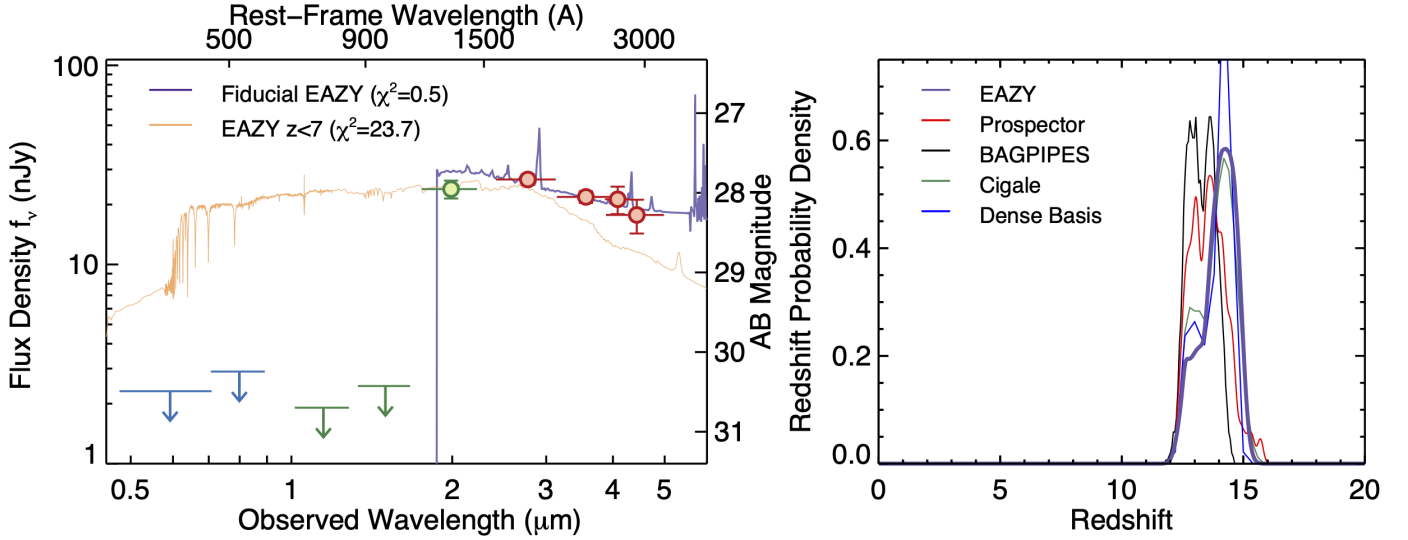
Figure 3. Left) The circles denote our fiducial photometry, with blue, green and red denoting *HST*/ACS, and NIRCam short and long-wavelength instruments, respectively. This SED exhibits the hallmark shape of a high-redshift galaxy, with several non-detections in blue filters, followed by significant detections with a blue spectral slope. The arrows denote 1σ upper limits. The F150W-F200W break color is >2.5 mag (1σ), which is sufficient to rule out all low-redshift solutions. The purple curve shows the best-fitting EAZY model at $z = 14.3$, which has an extremely good fit with $\chi^2 = 0.5$. The orange curve shows the result if we force EAZY to find a solution at $z < 7$. This model is unable to match the amplitude of the break as well as the slope redward of the break, and is correspondingly ruled out at high confidence ($\chi^2_{low-z} = 23.7$). Right) Photometric redshift probability distribution functions for Maisie's Galaxy. The thick purple curve shows the fiducial PDF from EAZY, which exhibits no low-redshift solution and a peak at $z = 14.3^{+0.4}_{-1.1}$. The remaining curves show the results from independent runs with PROSPECTOR, BAGPIPES, CIGALE and DENSE BASIS (see §5). All results significantly prefer a $z > 12$ solution, with all four codes finding best-fit redshifts nearly identical to EAZY ($z = 14.1^{+0.5}_{-0.4}$, $z = 13.6^{+0.4}_{-0.7}$, $z = 13.9^{+1.0}_{-1.0}$ and $z = 14.1^{+0.3}_{-1.1}$ respectively).

⁵⁴⁹ As an additional check, we measured photometry at the position of this source on our images without our post-processing residual background subtraction step, to ensure any systematic effects at this source position did not affect our results. The images already have a pedestal background subtracted in the pipeline, so the relative colors should be secure when measured in this way. We found that this set of photometry was consistent with our fiducial photometry, and EAZY returns $\int \mathcal{P}(z > 12) = 0.95$. Therefore it is unlikely that our sky subtraction routine negatively affected our result.

Dust-reddened foreground galaxies are another potential source of contamination. However, Maisie's Galaxy is not significantly detected in the deepest mid- and far-infrared, sub-millimeter and radio data available for this sky region, including Spitzer MIPS 24 μm (Magnelli et al. 2009), Herschel PACS 100 μm and 160 μm (Lutz et al. 2011), Herschel SPIRE 250μm, 350μm, and 500μm (Oliver et al. 2012), JCMT SCUBA2 850μm (Geach et al. 2017), and VLA 10 cm (Dickinson, priv. comm.).

4.2.1. *Stellar Screening*

Low-mass stars and brown-dwarfs can have colors that mimic high-redshift galaxies in broadband filters (e.g Yan et al. 2003; Ryan et al. 2005; Caballero et al. 2008; Wilkins et al. 2014) in the absence of longer wavelength observations ($\lambda_{\rm obs} \gtrsim 2\ m u$m). We explore this possibility following the methodology in Finkelstein et al. (2022). In brief, we derive a grid of models for the colors of low-mass stars and brown dwarfs (spectral types of M4–T8) in the NIRCam filters, by integrating the IRTF SpEX brown dwarf templates (Burgasser 2014). As these spectra end at 2.5μm, we use the tabulated 2MASS photometry to link each SpeX model with *Spitzer*/IRAC photometry from Patten et al. (2006). As the differences in filter transmission are negligible, we assume we can map IRAC 3.6μm onto F356W and 4.5μm onto F444W, however this assumption will need to be revisited with future spectroscopic observations of brown dwarfs with *JWST* at $\lambda \gtrsim 2.5\ \mu$m. We estimate the best brown dwarf template would be an L1-dwarf, and such a source would have blue near-infrared color of F150W−F200W < 0.75 mag. This is strongly ruled out by our observation of F150W−F200W>2.5 mag. Additionally, our size analysis in §5.2, which shows that this source is inconsistent with a point source.

Table 2. Measured Photometry of Maisie's Galaxy

F606W	F814W	F115W	F150W	F200W	F277W	F356W	F410M	F444W
1.26±2.31	0.4±2.9	−0.71±1.91	0.59±2.45	23.90±2.46	26.71±1.61	21.84±1.46	21.25±3.34	17.73±3.42

NOTE—Fluxes are in nJy. AB magnitudes can be derived via: $-2.5 \log_{10} (f_\nu[\mathrm{nJy}]) + 31.4$.

4.2.2. *Photometric Accuracy*

While our fiducial photometric measurements were derived in as robust a manner as possible, different software packages require different parameters and assumptions, which could lead to unknown systematic biases. We thus independently derive NIRCam photometry from our images with two independent software packages. The first method is PHOTUTILS from Python's astropy package (Bradley et al. 2020). Source detection was performed on a combined F277W and F356W image and the resulting segmentation image passed to the PHOTUTILS SourceCatalog routine, which carried out aperture-matched photometry on the background-subtracted, PSF-matched images in each filter.

The second method is a custom photometry package, where photometry is measured in circular apertures with radii ranging from $0.10''$ to $0.35''$, applying aperture corrections for point-like sources (<0.1 mag for r$>0.25''$), and after locally ($30''$ box) aligning the images (Pérez-González et al. 2008). Sky noise measurements in a $6'' \times 6''$ box around the source take into account correlated noise and are used to quote 5σ upper limits for non-detections. Photometric differences for each band are smaller than 0.1 mag for apertures between $0.2''$ and $0.35''$, 0.3-0.6 mag fainter for smaller radii, indicating that the source is (slightly) resolved. This method was applied to the non-PSF-matched imaging.

Comparing results between our fiducial SE photometry and these independent methods, we find extremely high consistency. The ratio between our fiducial fluxes and these photometry values in the four broadbands with significant detections is within 5–15%. The upper limits in F115W and F150W are similar to our fiducial values. The F150W−F200W Lyman-α break colors were >2.9 and >2.5 mag from PHOTUTILS and the custom method, respectively. These are the same or stronger than our fiducial values, as both methods find a somewhat stronger F200W flux than we find, possibly due to the use of the non-PSF matched images. Comparing colors, our measured F277W−F356W color of -0.2 ± 0.3 is in between, and consistent with, these two codes values of -0.1 ± 0.2 (PHOTUTILS) and -0.4 ± 0.3 (custom). We conclude that while differences in photometric packages and associated assumptions can affect the photometry at the $\sim 10\%$ level, this does not affect the validity of our candidate as these independent methods find a consistently strong Lyman-α break followed by a blue spectral slope, fully consistent with our interpretation of a $z \sim 14$ galaxy.

4.2.3. *Photometric Redshift Accuracy*

Similar to photometry, different photometric redshift packages can also impart biases on results. While we have used a well-tested fiducial package in EAZY, and implemented a new set of templates customized for very high-redshift galaxies, it is prudent to explore whether other packages would find different photometric redshift results. As we discuss below, we have run the PROSPECTOR (Johnson et al. 2021), BAGPIPES (Carnall et al. 2018), CIGALE (Burgarella et al. 2005; Noll et al. 2009; Boquien et al. 2019) and DENSE BASIS (Iyer & Gawiser 2017; Iyer et al. 2019) SED-fitting codes on our fiducial photometry. While for the stellar population properties discussed below, we use our EAZY-derived $\mathcal{P}(z)$ as a redshift prior, we also performed an independent run with the redshift as a free parameter. Figure 3 shows our fiducial EAZY $\mathcal{P}(z)$ along with the redshift PDFS from these independent runs.

These five results show remarkable consistency, all preferring $z > 12$ with no significant low-redshift solutions. All four codes find results simular to our fiducial EAZY run. PROSPECTOR finds $z = 14.1^{+0.5}_{-0.4}$, BAGPIPES finds $z = 13.3^{+0.5}_{-0.7}$, CIGALE finds $z = 13.9^{+1.0}_{-1.0}$, and DENSE BASIS finds $14.10^{+0.32}_{-1.10}$. Combining the posteriors of all four photometric redshift estimates provides a redshift PDF in agreement with our fiducial EAZY results with a median redshift of 13.8, and a 97.5% confidence that $z > 12.4$. We conclude that systematic biases due to choices in photometric redshift analyses are not affecting our results. Our fiducial result uses that from EAZY as it used templates trained on observations, while the full grids spanned by the other four codes may include nonphysical parameter combinations.

4.2.4. *Contamination Estimation*

To determine the likelihood that our selection criteria would produce a low-redshift contaminant we imposed
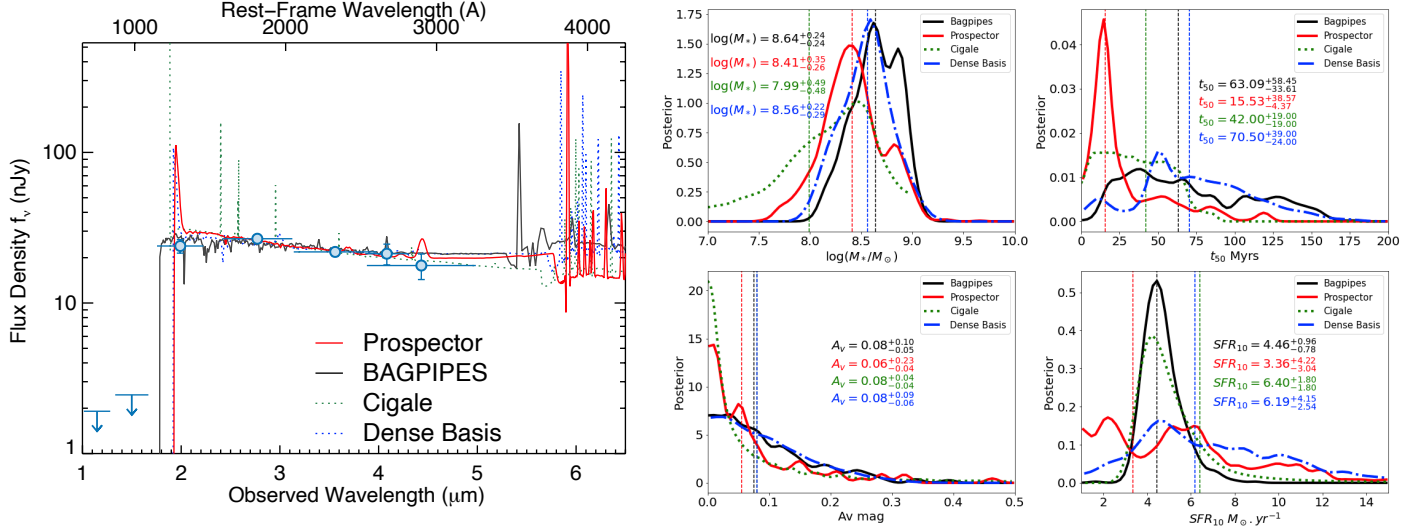
Figure 4. Left) Plot showing our fiducial photometry of Maisie's Galaxy alongside best-fit SED models from the SED fitting code PROSPECTOR (red line; fiducial, see Table 1), BAGPIPES (black), CIGALE (green dotted) and DENSE BASIS (blue dotted). Right) Posterior distributions of the key stellar population properties from all four codes. The panels show stellar mass, mass weighted age, dust attenuation and SFR averaged over the last 10 Myrs. The vertical dotted lines indicate the mean of the posteriors. Posteriors of attenuation are consistent between all four codes. PROSPECTOR prefers a younger age than the other three because of a recent burst in the SFH of this object. As a consequence of the burst, PROSPECTOR also estimates a lower SFR. The four estimates of the stellar mass posteriors exhibit significant overlap, though the median values differ by $\pm$ 0.4 dex. Future observations in the rest-optical with MIRI could break these degeneracies.

our same selection criteria cuts on the simulated catalogs used for all the mock CEERS observations. We note that there are zero $z > 10$ sources in this catalog so recovery of any source using these selection criteria would indicate contamination of our high-redshift sample. More information about the simulation used can be found in Yung et al. (2022) and Somerville et al. (2021). We use the perturbed fluxes as described in Larson et al. (2022, in prep) which use the same method as determined by Bagley et al. (2022, in prep) where they modeled the noise in simulated *JWST* images to have a Voigt profile distribution. We used the 1σ-depth in each filter for our errors and ran the whole catalog through EAZY. As our catalog-level fluxes do not have aperture-specific fluxes we cannot impose criteria based on those fluxes. We apply the following selection criteria to the simulated catalog: SNR in both F200W and F277W > 6, $\int \mathcal{P}(z > 8) \geq 0.9$, $z_{best} > 8.5$, $\chi^2_{EAZY} < 20$, SNR ≤ 1.5 in F606W & F814W & F115W & F150W, F200W magnitude < 29, F200W-F444W color < 1, and $\chi^2_{Low-z} - \chi^2_{fiducial} > 4$. Finally, matching the values to those of Maisie's Galaxy, which exhibits SNR > 10 in both F200W and F277W and $\int \mathcal{P}(z > 12) \geq 0.99$, we find zero sources that meet our criteria. This provides further evidence that Maisie's Galaxy has a high-redshift nature.

4.2.5. *CANDELS WFC3 Images*

Given the much greater sensitivity of NIRCam, we do not expect to detect this source in *HST* WFC3 IR images. These images were not included in our fiducial SE analysis as they had not yet been pixel aligned given the short time since NIRCam data acquisition. However, upon inspection we find a hint of a positive signal at the position of the source in the F160W image. Indeed, while the source is not in in the published Stefanon et al. (2017) and Skelton et al. (2014) catalogs, there is a 3.5σ detection at a separation of 0.15″ in the Finkelstein et al. (2022) catalog (this catalog has SNR < 2 in all other *HST* filters).

Using SE we perform forced photometry at this position on the CANDELS 60 mas images, and measure a flux of 10.1 ± 3.0 nJy in a 0.2″-diameter aperture, and 25.2 ± 7.3 nJy in a 0.4″-diameter aperture, consistent with the SNR from the Finkelstein et al. (2022) catalog. Tests placing 20,000 random non-overlapping apertures of size 0.2, 0.3 and 0.4″ in blank-sky regions of the F160W images (identifed by the segmentation map) yield fluxes of this level or higher roughly 5% of the time, consistent with this being roughly a 3σ detection in a noise distribution with non-Gaussian tails (similar 5% spurious rates were found in several independant tests).

While this flux may thus be spurious in origin, we explore how our results would change if it is astrophysical. We re-measured the photometric redshift using all *HST* measurements from the Finkelstein et al. (2022) catalog.

The resulting $\mathcal{P}(z)$ is bimodal, with a peak at our fiducial redshift of $z \sim 14$–15, and another at $z \sim 12.5$–13. The majority of the probability density (67%) is still at $z > 13$. This secondary redshift solution could be explained by a very strong Lyα emission line in the ~ 100 Å window between the red cutoff of the F150W and F160W filters at $\sim 1.68\mu$m ($z \sim 12.8$). Such a line would need to have a rest-frame equivalent width $\gtrsim 300$Å, well in excess of any observed source even much later in the epoch of reionization (e.g. Jung et al. 2020; De Barros et al. 2017; Pentericci et al. 2018). Whether this source is truly a "run-of-the-mill" $z \sim 14$ galaxy, or an exceptional $z \sim 13$ galaxy in an early ionized bubble, either would be an exciting and unexpected discovery.

Due to the low signal-to-noise of the F160W detection coupled with the updated photometric redshift continuing to prefer $z \sim 14$ over $z \sim 13$, and the extreme low likelihood that such an extreme object would happen to reside in our field at a precise redshift to create this F160W signal, we use our fiducial (non-*HST*) photometric redshifts for the remainder of this paper. Future work with pixel-aligned *HST*+NIRCam mosaics will improve this methodology.

5. DISCUSSION

5.1. *Physical Properties*

The five photometric detections afforded by NIRCam allow us the unprecedented opportunity to study the physical properties of a galaxy potentially only ~ 300 Myr after the Big Bang. Our fiducial stellar population modeling is done with the Prospector Bayesian SED fitting code (Johnson et al. 2021). We follow the same procedures as in Tacchella et al. (2022) and we refer the reader there for more details. Briefly, we model the SED with a 13-parameter model that includes redshift (prior is set to the posterior of Eazy), stellar mass, stellar and gas-phase metallicities, dust attenuation (two-component dust model including birth-cloud dust attenuating young stars (< 10 Myr) and nebular emission, a diffuse component for the whole galaxy with a flexible attenuation law; 3 parameters), and an ionization parameter for the nebular emission. We adopt a flexible SFH prescription with 6 time bins (the first two look-back time bins are spaced at $0 - 5$ Myr and $5 - 10$ Myr, while the other four are log-spaced out to $z = 20$; 5 free parameters) and with the bursty-continuity prior. Furthermore, we assume the MIST stellar models (Choi et al. 2017) and a Chabrier (2003) IMF.

To explore how robust these properties are, we perform an independent fit with the Bayesian Bagpipes (Carnall et al. 2018), Cigale (Burgarella et al. 2005; Noll et al. 2009; Boquien et al. 2019) and Dense Ba-

sis (Iyer & Gawiser 2017; Iyer et al. 2019) SED-fitting codes. For Bagpipes we assumed a simple exponential star formation history with a Chabrier IMF, a Calzetti dust attenuation law and included nebular emission with an ionization parameter of 10^{-3}, with Bruzual & Charlot (2003) stellar population models. For Cigale, we assume a delayed star formation history after checking that adding a burst does not significantly modify the results. Bruzual & Charlot (2003) models with a Chabrier IMF and was used. Dense Basis was run using the flexible non-parametric SFH model and priors described in Iyer et al. (2019), assuming a Calzetti dust law and a Chabrier IMF.

The marginalized posterior values of the inferred physical properties from Prospector are summarized in Table 1 and Fig. 4. We infer a stellar mass of $\log(M_*/M_\odot) = 8.5^{+0.3}_{-0.3}$. The attenuation in this galaxy is rather low with $A_V = 0.06^{+0.23}_{-0.04}$ mag, though we stress that this is not well constrained because we only fit the rest-UV and it is degenerate with the slope of the attenuation law (which is variable in this fit). However, the low dust attenuation is in agreement with the measured UV spectral slope $\beta = -2.32^{+0.11}_{-0.20}$ (measured using the same techniques as in Tacchella et al. 2022). This blue color implies little dust, though does not require extremely low metallicities (e.g. Finkelstein et al. 2012; Dunlop et al. 2013; Bouwens et al. 2014). Interestingly, this galaxy is about as blue as $z \sim 7$ galaxies of similar mass (Finkelstein et al. 2012), implying little evolution in chemical enrichment between these two epochs.

We infer a SFR$_{10}$ (average of the past 10 Myr[6]) of 4 M$_\odot$ yr^{-1} and the corresponding sSFR$_{10}$ is $10^{-7.9}$ yr^{-1}. By looking at the posterior distribution of the SFH, it becomes apparent that the model for this galaxy had an episode of elevated star formation $10 - 20$ Myr ago with a SFR of 6^{+22}_{-4} M$_\odot$ yr^{-1}, i.e. the SFR has been slightly decreasing in the recent 10 Myr. This explains the mass-weighted age of 16^{+45}_{-6} Myr. This is also consistent with the half-mass formation time of dark matter halos at $z \sim 14$ of a few tens of Myr (Tacchella et al. 2018).

These Prospector-based posterior distributions are consistent with the ones from Bagpipes, Cigale and Dense Basis (see Fig. 4), though the difference in age is large (age is defined at half-mass time, t_{50}, which is close to the mass-weighted age). Bagpipes, Cigale and Dense Basis prefer higher age values (although the posterior distributions are also broader) with 63^{+33}_{-58}

---

[6] Although the SFR$_{10}$ would be best estimated from nebular emission lines, the (F)UV actually also probes such short timescales, in particular for bursty star formation (e.g. Caplar & Tacchella 2019; Flores Velázquez et al. 2021) expected at these redshifts.

Myr, 42 ± 19 Myr, and $70.5^{+24.0}_{-39.0}$ Myr respectively. The SFH inferred from Dense Basis shows a recent burst of star formation in the last ~ 30 Myr. The larger mass-weighted age comes from the long tail of low-level star formation in the galaxy leading up to the recent burst. The spread in these results could be explained by differences in SFHs (e.g., non-parametric versus parametric), and also the lack of observational constraints in the rest-frame optical.

Several pre-*JWST* studies have focused on inferring SFHs and stellar ages of $z \approx 8 - 10$ galaxies (e.g. Hashimoto et al. 2018; Laporte et al. 2021; Stefanon et al. 2022). Specifically, Tacchella et al. (2022) – using Prospector with the same bursty continuity prior – found a diversity of stellar ages, ranging from 10 Myr to 260 Myr, and stellar masses ($10^9 - 10^{11}$ M$_\odot$), with more massive galaxies being older. In particular the galaxies at $z \approx 9 - 10$ with stellar masses at the higher end and the older ages ($t_{50} \approx 100$ Myr) are consistent with being the descendants of Maisie's Galaxy. Recently, Naidu et al. (2022) inferred the properties of two galaxies at $z \approx 10.6$ and $z \approx 12.4$ (see also Castellano et al. 2022) with Prospector and a similar setup, allowing us do a useful comparison. Their two galaxies have $\log(M_*/M_\odot) = 9.4^{+0.3}_{-0.3}$ and $9.0^{+0.3}_{-0.4}$, SFR$_{50\mathrm{Myr}} = 12^{+9}_{-4}$ M$_\odot$ yr^{-1} and 7^{+4}_{-3} M$_\odot$ yr^{-1}, and $t_{50} = 111^{+43}_{-54}$ Myr and 71^{+33}_{-32} Myr, respectively. This is older than what we infer for our galaxy, though this age difference could be explained by the stellar mass difference, along with the higher preferred redshift for Maisie's Galaxy. Importantly, detailed stellar population analyses of early galaxies will advance significantly with *JWST*, in particular when including spectroscopic information.

5.2. *Source Morphology*

We derive the sizes of Maisie's Galaxy using two morphological fitting codes, Galfitm[7] (Häußler et al. 2013) and statmorph[8] (Rodriguez-Gomez et al. 2019). Galfitm is a modified version of Galfit[9] (Peng et al. 2002; Peng et al. 2010), a least-squares fitting algorithm that finds the optimum Sérsic fit to a galaxy's light profile. We perform fits using Galfitm by allowing the Sérsic index to vary between 0.01 and 8, the magnitude of the galaxy between 0 and 45, and r_{half} between 0.3 and 200 pixels (on our $0.03''$ pixel scale). As input, we use a 100×100 pixel cutout of the F200W science image, the segmentation map created by Source Ex-

tractor, and the empirical PSF measured from our CEERS2 pointing, which we allow Galfitm to oversample relative to the data by a factor of nine. We estimate the uncertainty on our fits by conducting a Monte Carlo analysis where we modify the input F200W science image to randomly vary the pixel-to-pixel noise, recompute the parameters, and then repeat this analysis 40 times.

Following this procedure, we measure a half-light radius of 3.3 ± 0.3 pixels ($0.1 \pm 0.01''$), which corresponds to a physical size of 330 ± 30 pc at $z = 14$. We check these results using the standard configuration of Statmorph, a Python package developed to calculate the nonparametric morphology of galaxies as well as compute single Sérsic fits. Using the same images as input, we find a half-light radius of 3.9 pixels, in good agreement with the measurement from Galfitm. We repeat this measurement for the F277W filter and a stacked F200W+F277W image and find consistent results. The measured half-light radius of 3.3 ± 0.3 is significantly larger than that expected for a point-source (the median r_h for our PSF stars is 1.8 ± 0.3 pixels), further ruling out a stellar origin for this source.

5.3. *Comparison to Model Predictions*

In Figure 5 we present predictions from a range of theoretical models, including the First Light And Reionisation Epoch Simulations (FLARES, Lovell et al. 2021; Vijayan et al. 2021; Wilkins et al. 2022), a suite of hydrodynamical cosmological zoom simulations; the large periodic volume hydrodynamical simulation Bluetides (Feng et al. 2016; Wilkins et al. 2017); the Delphi (Dayal et al. 2014, 2022) and Santa Cruz SAM (Yung et al. 2019, 2020) semi-analytical models, the semi-empirical UniverseMachine (Behroozi et al. 2020), Mason et al. (2015), and Behroozi & Silk (2015) models. For the FLARES, Delphi, and Behroozi & Silk (2015) models, we show both the attenuated and un-attenuated (intrinsic) predictions. These predictions were made by interpolating and integrating either the binned or Schechter luminosity functions across $z = 15 \rightarrow 13$ taking account of the areal size of the CEERS observations. Almost all of these models predict an expected source density much less than one, making the observation of even a single object at this redshift and magnitude surprising and potentially hinting at significant differences between the physical assumptions in these models and the real early universe.

The exception is the Behroozi & Silk (2015) model, which extrapolated galaxy formation to high redshifts by assuming that the ratio between galaxies' sSFRs and their host halos' specific accretion rates remained con-

---

[7] https://www.nottingham.ac.uk/astronomy/megamorph/

[8] https://statmorph.readthedocs.io/en/latest/

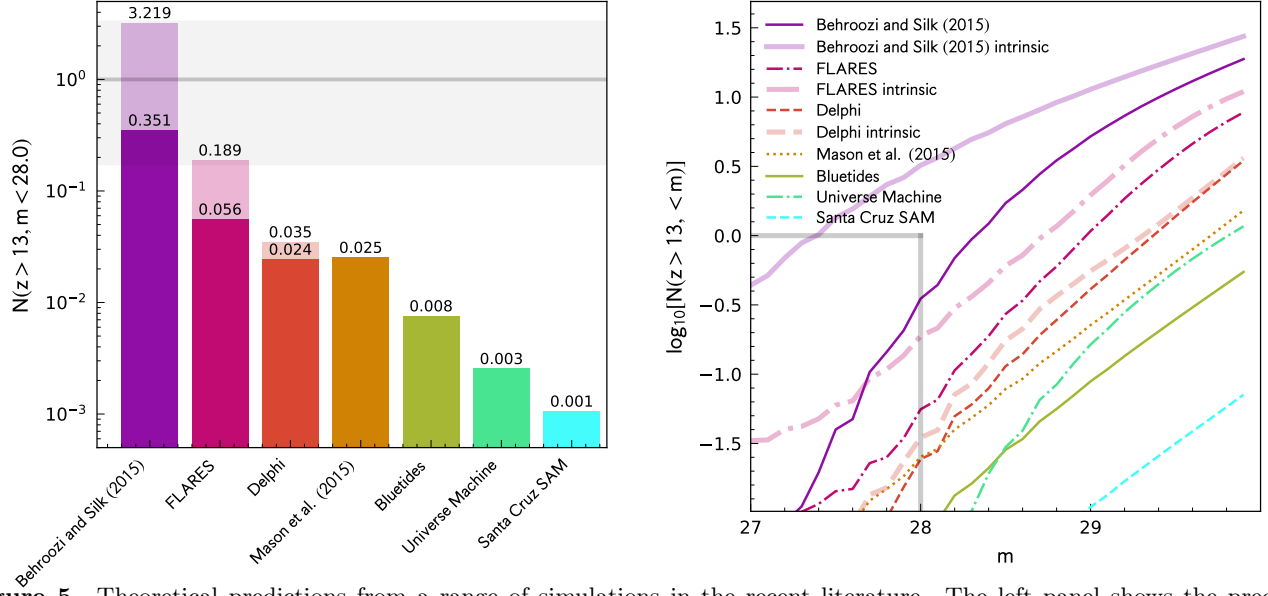[9] https://users.obs.carnegiescience.edu/peng/work/galfit/galfit.html

Figure 5. Theoretical predictions from a range of simulations in the recent literature. The left panel shows the predicted number of sources at $m < 28$ (the approximate brightness of our source) and $13 < z < 15$ over our survey area of 34.5 sq. arcmin. The vertical axis and the values above each bar give the number predicted. Dark (light) shading denotes the value derived from models with (without) dust attenuation applied. The right panel shows these same theoretical predictions, now showing the cumulative number as a function of apparent magnitude. The bulk of these models predict that $m \sim 28$ galaxies at $z > 13$ are not highly likely, though the Behroozi & Silk (2015) model, which has no accelerated decline in the cosmic SFR density at $z > 8$, has the least tension. However, our detection of one source has a large Poisson (and cosmic variance) uncertainty (gray shading in the left panel), so strong conclusions cannot yet be made.

stant, which they showed was equivalent to assuming that galaxies' stellar masses are proportional to a power of their host halo masses. This model was constrained only with observational data at $z \le 8$, and predicted no change in the slope of the CSFR relation with redshift at $z > 8$. As a result, it predicted many more high-redshift galaxies than later models that were constrained to match $z \sim 9$ and ~ 10 data from *HST* that suggested more rapid declines in the number densities of early galaxies. We caution against over-interpretation, as the current sample contains only a single object with a consequently large Poisson error in addition to additional uncertainty due to cosmic variance. Nevertheless, if confirmed, the existence of this object places informative constraints on galaxy formation models in this epoch.

5.4. *Comparisons to Extrapolations from Lower Redshift*

We are now only just getting our first glimpse into this epoch with the first *JWST* data. Nonetheless, we can compare our observed number density to a few recent observations. We calculate a rough number density for $M_{UV} = -20$ galaxies assuming a top-hat selection function over $12 < z < 15$. This is overly simplistic, and does not account for incompleteness (which, although this is a $>10\sigma$ detection, certainly is non-unity due to our strin-

gent selection criteria). Nonetheless it is illustrative of a rough number density. We find a maximum volume over the CEERS first-epoch area of 1.33×10^5 Mpc^3, for a number density for our singular source of $7.5^{+9.5}_{-1.3} \times 10^{-6}$ Mpc^{-3} (where the uncertainties are Poisson based on our detection of one object).

We illustrate this number density in Figure 6. Our derived number density is not inconsistent with a variety of observational constraints at $z \sim 10$, as well as recent results at $z \sim 12$–13. The solid gray line shows the predicted $z = 14$ Schechter function from Finkelstein (2016), which is extrapolated from an empirical fit to observations at $z = 4$–8, assuming smooth redshift evolution. Interestingly, our rough number density measurement is in excellent agreement with this prediction, which would support its assumption of a smooth decline in the luminosity function (and in the corresponding star-formation rate density). We show a double-power law (DPL) evolving model, here at $z = 12$, from Finkelstein & Bagley (2022). This is also consistent with our results at the faint end.

As noted by several previous studies the bright-end of the luminosity function at $z \ge 9$ exhibits an interesting excess over predicted levels (e.g. Bowler et al. 2020; Rojas-Ruiz et al. 2020; Morishita et al. 2018; Bagley et al. 2022; Finkelstein et al. 2022). While our survey
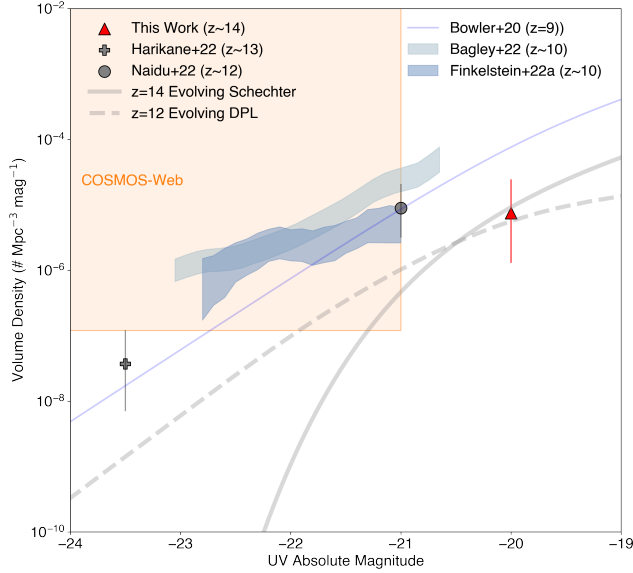
Figure 6. A view on the luminosity function at $z \geq 10$. The shaded light blue regions show observational constraints at $z \sim 10$ Bagley et al. (2022); Finkelstein et al. (2022), while the thin line shows the $z = 9$ DPL luminosity function from Bowler et al. (2020). The remaining points show $z > 12$ results from this work (triangle), the ground-based work of Harikane et al. (2022), and the recent *JWST* work of Naidu et al. (2022). The thick lines show empirical luminosity function models which evolve smoothly with redshift, with the solid line denoting a Schechter function evolved to $z = 14$ (Finkelstein 2016), and the dashed line a DPL evolved to $z = 12$ (Finkelstein & Bagley 2022). The constraints placed by our observations on the faint-end of the luminosity function are consistent with a smooth decline out to $z \sim 14$. However, brighter observations are still in excess of the bright-extension of these smoothly-declining functions. The shaded box shows the parameter-space reached by the upcoming COSMOS-Web survey, which will probe the very bright end at these redshifts.

area does not yet probe the volume densities needed to reach these brighter potential $z = 14$ galaxies, if the high-redshift luminosity function follows a DPL form, the forthcoming 0.6 deg^2 COSMOS-Web survey (PIs Kartaltepe & Casey) should be able to discover this population. In combination with the full Cycle 1 slate of surveys, including the completed CEERS imaging, it will afford a more complete view of the $z = 14$ universe.

6. CONCLUSIONS

We present the results from a search for ultra-high-redshift galaxy candidates from the first epoch of NIR-Cam imaging from the *JWST* CEERS survey. We use imaging from both the short and long-wavelength cameras over four pointings, covering 34.5 sq. arcmin in the F115W, F150W, F200W, F277W, F356W, F410W and F444W filters, reaching $m \sim 29$ (5σ) in the deepest bands. We measure photometry using SOURCE EXTRACTOR, with an emphasis on robust measurements of colors, total fluxes, and uncertainties.

We estimate photometric redshifts with the EAZY software package, including new blue templates designed to better recover the colors of very distant galaxies. We develop iteratively a set of conservative selection criteria to select candidate galaxies at $z > 12$. We find an initial sample of nine candidate galaxies, with only one candidate galaxy satisfying stringent non-detections (SNR <1.5) in all dropout bands, and detected at $>10\sigma$ in the detection bands.

This object, dubbed Maisie's Galaxy, has a photometric redshift of $14.3^{+0.4}_{-1.1}$, and was found in the CEERS2 field. We explored all known potential sources of contamination, including instrumental effects, systematic biases in the analysis, and contamination by lower-redshift galaxies or Galactic stars. We find that none of these alternative explanations can account for the observations, leaving us with the conclusion that it is a robust $z \sim 14$ galaxy candidate.

We explore the physical properties of this unexpected galaxy. As might be expected for such an early epoch, this galaxy is blue, with a UV spectral slope $\beta = -2.3$, consistent with low levels of dust attenuation. Stellar population modeling with multiple codes are in agreement that this source has a modest stellar mass of log $(M/M_\odot) \sim 8.5$, with a high log sSFR of -7.9 yr^{-1}. The mass-weighted age of Maisie's Galaxy is young, with a median of ~ 20 Myr, though stellar populations as old as 150 Myr ($z_{form} > 20$) cannot be ruled out. The galaxy candidate is significantly resolved, with $r_h = 3.3 \pm 0.3$ pixels, for a physical size of ~ 330 pc at $z = 14$.

We compare the abundance of this single galaxy both to model predictions and previous observations. We find that the presence of this source is unexpected based on most model predictions, though given our sample size the tension is modest at best. However, both semi-empirical models and empirical extrapolations, which assume a smooth decline in the SFR density at $z > 8$, predict volume densities of such $z \sim 14$ sources in agreement with our observations. Should more such sources be found in early *JWST* surveys, it would provide further evidence against accelerated decline SFR density scenarios.

Such a galaxy population would also present challenges for a variety of dark matter models with suppressed power on small scales, such as fuzzy dark matter (e.g. Sullivan et al. 2018), and possibly even for standard ΛCDM models. Additionally, the presence of this galaxy ~ 300 Myr after the Big Bang may be consistent

with redshifted 21-cm absorption at $z \sim 18$ reported by the Experiment to Detect the Global Epoch of Reionization Signature (EDGES Bowman et al. 2018), and reported to be caused by light from the first stars.

We note that this source has a low significance detection in *HST* F160W. Our tests show that this signal may be spurious, but if it is astrophysical in origin, it would indicate an extraordinary galaxy at $z \sim 13$ with a rest-frame Lyα equivalent width of >300 Å. Such an object would necessitate an extreme (e.g. Malhotra & Rhoads 2002) stellar population (very low metallicity, or a very early accreting super-massive black hole) residing in an unprecedentedly early ionized bubble, an equally exciting result.

We caution the reader that this galaxy is a candidate. While we have exhausted multiple avenues to explore whether its presence in our data could be caused by instrumental effects, whether our measurement techniques were biased, or whether its colors could be consistent with lower-redshift sources, the "gold standard" of distance measurements is spectroscopic confirmation. Such confirmation should be possible in modest exposure times with the NIRSpec and/or MIRI spectrographs on board *JWST*. The combination of larger samples being compiled by *JWST* Cycle 1 programs, including the remainder of CEERS, COSMOS-Web (PIs Kartaltepe & Casey), JADES (PIs Rieke & Ferruit), PRIMER (PI Dunlop), PEARLS (Windhorst et al., in prep) and NGDEEP (PIs Finkelstein, Papovich, & Pirzkal) coupled with subsequent spectroscopic followup will further illuminate the earliest phases of galaxy formation.

Software: Astropy (Astropy Collaboration et al. 2013), Bagpipes (Carnall et al. 2018), Cigale (Burgarella et al. 2005; Noll et al. 2009; Boquien et al. 2019), Dense Basis (Iyer & Gawiser 2017; Iyer et al. 2019), Drizzle (Fruchter & Hook 2002), eazy (Brammer et al. 2008), GalfitM (Peng et al. 2010; Häußler et al. 2013), Photutils (Bradley et al. 2020), Prospector (Johnson et al. 2021), SciPy (Virtanen et al. 2020), Source Extractor (Bertin & Arnouts 1996), Statmorph (Rodriguez-Gomez et al. 2019), STScI *JWST* Calibration Pipeline (jwst-pipeline.readthedocs.io)

REFERENCES

Astropy Collaboration, Robitaille, T. P., Tollerud, E. J., et al. 2013, A&A, 558, A33

Bagley, M. B., Finkelstein, S. L., Rojas-Ruiz, S., et al. 2022, arXiv e-prints, arXiv:2205.12980

Behroozi, P., Conroy, C., Wechsler, R. H., et al. 2020, MNRAS, 499, 5702

Behroozi, P. S., & Silk, J. 2015, ApJ, 799, 32

Bertin, E., & Arnouts, S. 1996, A&AS, 117, 393

Boquien, M., Burgarella, D., Roehlly, Y., et al. 2019, A&A, 622, A103

Bouwens, R. J., Illingworth, G. D., Oesch, P. A., et al. 2014, ApJ, 793, 115

—. 2015, ApJ, 803, 34

Bouwens, R. J., Oesch, P. A., Stefanon, M., et al. 2021, AJ, 162, 47

Bowler, R. A. A., Jarvis, M. J., Dunlop, J. S., et al. 2020, MNRAS, 493, 2059

Bowman, J. D., Rogers, A. E. E., Monsalve, R. A., Mozdzen, T. J., & Mahesh, N. 2018, Nature, 555, 67

Bradley, L., Sipőcz, B., Robitaille, T., et al. 2020, astropy/photutils: 1.0.0, Zenodo

Brammer, G. B., van Dokkum, P. G., & Coppi, P. 2008, ApJ, 686, 1503

Bruzual, G., & Charlot, S. 2003, MNRAS, 344, 1000

Burgarella, D., Buat, V., & Iglesias-Páramo, J. 2005, MNRAS, 360, 1413

Burgasser, A. J. 2014, in Astronomical Society of India Conference Series, Vol. 11, Astronomical Society of India Conference Series, 7–16

Caballero, J. A., Burgasser, A. J., & Klement, R. 2008, A&A, 488, 181

Caplar, N., & Tacchella, S. 2019, MNRAS, 487, 3845

Cardelli, J. A., Clayton, G. C., & Mathis, J. S. 1989, ApJ, 345, 245

Carnall, A. C., McLure, R. J., Dunlop, J. S., & Davé, R. 2018, MNRAS, 480, 4379

Casertano, S., de Mello, D., Dickinson, M., et al. 2000, AJ, 120, 2747

Casey, C. M., Scoville, N. Z., Sanders, D. B., et al. 2014, ArXiv e-prints

Castellano, M., Fontana, A., Treu, T., et al. 2022, arXiv e-prints, arXiv:2207.09436

Chabrier, G. 2003, PASP, 115, 763

Choi, J., Conroy, C., & Byler, N. 2017, ApJ, 838, 159

Coe, D., Zitrin, A., Carrasco, M., et al. 2013, ApJ, 762, 32

Dayal, P., & Ferrara, A. 2018, PhR, 780, 1

Dayal, P., Ferrara, A., Dunlop, J. S., & Pacucci, F. 2014, MNRAS, 445, 2545

Dayal, P., Ferrara, A., Sommovigo, L., et al. 2022, MNRAS, 512, 989

De Barros, S., Pentericci, L., Vanzella, E., et al. 2017, A&A, 608, A123

Dunlop, J. S., Rogers, A. B., McLure, R. J., et al. 2013, MNRAS, 432, 3520

Feng, Y., Di-Matteo, T., Croft, R. A., et al. 2016, MNRAS, 455, 2778

Finkelstein, S. L. 2016, PASA, 33, e037

Finkelstein, S. L., & Bagley, M. B. 2022, arXiv e-prints, arXiv:2207.02233

Finkelstein, S. L., Papovich, C., Salmon, B., et al. 2012, ApJ, 756, 164

Finkelstein, S. L., Ryan, Jr., R. E., Papovich, C., et al. 2015, ApJ, 810, 71

Finkelstein, S. L., Bagley, M., Song, M., et al. 2022, ApJ, 928, 52

Flores Velázquez, J. A., Gurvich, A. B., Faucher-Giguère, C.-A., et al. 2021, MNRAS, 501, 4812

Fruchter, A. S., & Hook, R. N. 2002, PASP, 114, 144

Geach, J. E., Dunlop, J. S., Halpern, M., et al. 2017, MNRAS, 465, 1789

Gnedin, N. Y. 2016, ApJL, 825, L17

Grogin, N. A., Kocevski, D. D., Faber, S. M., et al. 2011, ApJS, 197, 35

Hainline, K. N., Hviding, R. E., Rieke, M., et al. 2020, ApJ, 892, 125

Harikane, Y., Inoue, A. K., Mawatari, K., et al. 2022, ApJ, 929, 1

Hashimoto, T., Laporte, N., Mawatari, K., et al. 2018, Nature, 557, 392

Häußler, B., Bamford, S. P., Vika, M., et al. 2013, MNRAS, 430, 330

Iyer, K., & Gawiser, E. 2017, ApJ, 838, 127

Iyer, K. G., Gawiser, E., Faber, S. M., et al. 2019, ApJ, 879, 116

Jiang, L., Kashikawa, N., Wang, S., et al. 2021, Nature Astronomy, 5, 256

Johnson, B. D., Leja, J., Conroy, C., & Speagle, J. S. 2021, ApJS, 254, 22

Jung, I., Finkelstein, S. L., Dickinson, M., et al. 2020, ApJ, 904, 144

Koekemoer, A. M., Faber, S. M., Ferguson, H. C., et al. 2011, ApJS, 197, 36

Laporte, N., Meyer, R. A., Ellis, R. S., et al. 2021, MNRAS, 505, 3336

Lovell, C. C., Vijayan, A. P., Thomas, P. A., et al. 2021, MNRAS, 500, 2127

Lutz, D., Poglitsch, A., Altieri, B., et al. 2011, A&A, 532, A90

Madau, P., & Dickinson, M. 2014, ARA&A, 52, 415

Magnelli, B., Elbaz, D., Chary, R. R., et al. 2009, A&A, 496, 57

Malhotra, S., & Rhoads, J. E. 2002, ApJL, 565, L71

Mason, C. A., Trenti, M., & Treu, T. 2015, ApJ, 813, 21

McLeod, D. J., McLure, R. J., & Dunlop, J. S. 2016, MNRAS, 459, 3812

Morishita, T., Trenti, M., Stiavelli, M., et al. 2018, ApJ, 867, 150

Naidu, R. P., Oesch, P. A., van Dokkum, P., et al. 2022, arXiv e-prints, arXiv:2207.09434

Noll, S., Burgarella, D., Giovannoli, E., et al. 2009, A&A, 507, 1793

Oesch, P. A., Bouwens, R. J., Illingworth, G. D., Labbé, I., & Stefanon, M. 2018, ApJ, 855, 105

Oesch, P. A., Brammer, G., van Dokkum, P. G., et al. 2016, ApJ, 819, 129

Oke, J. B., & Gunn, J. E. 1983, ApJ, 266, 713

Oliver, S. J., Bock, J., Altieri, B., et al. 2012, MNRAS, 424, 1614

Papovich, C., Shipley, H. V., Mehrtens, N., et al. 2016, ApJS, 224, 28

Patten, B. M., Stauffer, J. R., Burrows, A., et al. 2006, ApJ, 651, 502

Peng, C. Y., Ho, L. C., Impey, C. D., & Rix, H.-W. 2002, AJ, 124, 266

Peng, C. Y., Ho, L. C., Impey, C. D., & Rix, H.-W. 2010, AJ, 139, 2097

Peng, C. Y., Ho, L. C., Impey, C. D., & Rix, H.-W. 2010, AJ, 139, 2097

Pentericci, L., Vanzella, E., Castellano, M., et al. 2018, ArXiv e-prints

Pérez-González, P. G., Rieke, G. H., Villar, V., et al. 2008, ApJ, 675, 234

Planck Collaboration, Aghanim, N., Akrami, Y., et al. 2020, A&A, 641, A6

Rigby, J., Perrin, M., McElwain, M., et al. 2022, arXiv e-prints, arXiv:2207.05632

Robertson, B. E. 2021, arXiv e-prints, arXiv:2110.13160

Rodriguez-Gomez, V., Snyder, G. F., Lotz, J. M., et al. 2019, MNRAS, 483, 4140

Rojas-Ruiz, S., Finkelstein, S. L., Bagley, M. B., et al. 2020, ApJ, 891, 146

Ryan, R. E., J., Hathi, N. P., Cohen, S. H., & Windhorst, R. A. 2005, ApJL, 631, L159

Schlawin, E., Leisenring, J., Misselt, K., et al. 2020, AJ, 160, 231

Skelton, R. E., Whitaker, K. E., Momcheva, I. G., et al. 2014, ApJS, 214, 24

Somerville, R. S., Olsen, C., Yung, L. Y. A., et al. 2021, MNRAS, 502, 4858

Stark, D. P. 2016, ARA&A, 54, 761

Stefanon, M., Bouwens, R. J., Illingworth, G. D., et al. 2022, arXiv e-prints, arXiv:2204.02986

Stefanon, M., Yan, H., Mobasher, B., et al. 2017, ApJS, 229, 32

Sullivan, J. M., Hirano, S., & Bromm, V. 2018, MNRAS, 481, L69

Tacchella, S., Bose, S., Conroy, C., Eisenstein, D. J., & Johnson, B. D. 2018, ApJ, 868, 92

Tacchella, S., Finkelstein, S. L., Bagley, M., et al. 2022, ApJ, 927, 170

Vijayan, A. P., Lovell, C. C., Wilkins, S. M., et al. 2021, MNRAS, 501, 3289

Virtanen, P., Gommers, R., Oliphant, T. E., et al. 2020, Nature Methods, 17, 261

Wilkins, S. M., Feng, Y., Di Matteo, T., et al. 2017, MNRAS, 469, 2517

Wilkins, S. M., Stanway, E. R., & Bremer, M. N. 2014, MNRAS, 439, 1038

Wilkins, S. M., Vijayan, A. P., Lovell, C. C., et al. 2022, arXiv e-prints, arXiv:2204.09431

Yan, H., Windhorst, R. A., & Cohen, S. H. 2003, ApJL, 585, L93

Yung, L. Y. A., Somerville, R. S., Finkelstein, S. L., Popping, G., & Davé, R. 2019, MNRAS, 483, 2983

Yung, L. Y. A., Somerville, R. S., Finkelstein, S. L., et al. 2020, MNRAS, 496, 4574

Yung, L. Y. A., Somerville, R. S., Ferguson, H. C., et al. 2022, arXiv e-prints, arXiv:2206.13521

Table 3. Information for Potential $z > 13$ Candidates

Catalog ID	RA	Dec	F200W	F277W	F606W	F814W	F115W	F150W	F200W	F277W
	(J2000)	(J2000)	(mag)	(mag)	SNR	SNR	SNR	SNR	SNR	SNR
Maisie's Galaxy	214.943153	52.942449	27.95	27.83	0.48	0.11	0.0	−0.4	11.9	18.5
CEERS–624	214.990084	53.003670	28.25	28.32	0.47	0.80	0.7	**1.9**	9.2	9.3
CEERS–608	214.905781	52.946391	26.74	26.87	**2.29**	-0.02	-0.3	**1.7**	12.4	10.7
CEERS–1173	214.891187	52.932738	26.81	26.86	-0.06	**1.67**	1.0	**1.7**	17.3	17.2
CEERS–2676	214.909694	52.937121	28.43	28.67	**1.78**	**1.60**	0.9	-0.5	16.4	11.6
CEERS–4868	214.908768	52.922180	28.08	28.01	**2.16**	**1.84**	1.3	0.5	13.4	11.3
CEERS–6772	214.775181	52.817152	27.42	27.67	-0.14	**2.07**	0.8	0.3	10.1	8.7
CEERS–11984	214.886659	52.829882	27.97	28.45	0.60	**3.15**	**1.5**	**1.7**	11.9	7.6
CEERS–971	214.867674	52.864955	28.38	28.34	0.44	-0.18	0.7	0.9	**7.4**	**8.1**

NOTE—SNRs were measured in $0.3''$-diameter apertures. Magnitudes quoted are corrected to total from the Kron aperture fluxes. The top row shows Maisie's Galaxy for comparison, while the remaining rows show the final set of objects removed when requiring SNR < 1.5 in a dropout band and the *HST*/ACS bands. The quantities in bold denote those responsible for removing the objects from the sample. This is typically due to SNR >1.5 in a dropout band. The exception is ID=971, which is a valid candidate, but was removed from the sample for this paper when we made a cut at SNR>10 in the detection bands to focus on only the most robust sources.

APPENDIX

Here we provide a table of the eight galaxy candidates (in addition to Maisie's Galaxy) which satisfied all except our final, most stringent set of selection criteria. In the table, we put in bold the quantity which resulted in the removal of a given object. Some of these objects may be true $z > 13$ galaxies, thus they are worthy of further study.

All Authors and Affiliations

Steven L. Finkelstein,[1] Micaela B. Bagley,[1] Pablo Arrabal Haro,[2] Mark Dickinson,[2] Henry C. Ferguson,[3] Jeyhan S. Kartaltepe,[4] Casey Papovich,[5,6] Denis Burgarella,[7] Dale D. Kocevski,[8] Marc Huertas-Company,[9,10,11] Kartheik G. Iyer,[12] Anton M. Koekemoer,[3] Rebecca L. Larson,[13,1] Pablo G. Pérez-González,[14] Caitlin Rose,[4] Sandro Tacchella,[15,16] Stephen M. Wilkins,[17,18] Katherine Chworowsky,[1,*] Aubrey Medrano,[1] Alexa M. Morales,[1] Rachel S. Somerville,[19] L. Y. Aaron Yung,[20] Adriano Fontana,[21] Mauro Giavalisco,[22] Andrea Grazian,[23] Norman A. Grogin,[3] Lisa J. Kewley,[24] Allison Kirkpatrick,[25] Peter Kurczynski,[26] Jennifer M. Lotz,[27] Laura Pentericci,[21] Nor Pirzkal,[28] Swara Ravindranath,[3] Russell E. Ryan Jr.,[3] Jonathan R. Trump[29] and Guang Yang[30,31]

and The CEERS Team:

Omar Almaini,[32] Ricardo O. Amorín,[33,34] Marianna Annunziatella,[35] Bren E. Backhaus,[36] Guillermo Barro,[37] Peter Behroozi,[38,39] Eric F. Bell,[40] Rachana Bhatawdekar,[41] Laura Bisigello,[42,23] Volker Bromm,[1] Véronique Buat,[7] Fernando Buitrago,[43,44] Antonello Calabrò,[45] Caitlin M. Casey,[1] Marco Castellano,[21] Óscar A. Chávez Ortiz,[1] Laure Ciesla,[7] Nikko J. Cleri,[5,6] Seth H. Cohen,[46] Justin W. Cole,[5,6] Kevin C. Cooke,[47] M. C. Cooper,[48] Asantha R. Cooray,[48] Luca Costantin,[35] Isabella G. Cox,[4] Darren Croton,[49,50] Emanuele Daddi,[51] Romeel Davé,[52,53] Alexander de la Vega,[54] Avishai Dekel,[55] David Elbaz,[56] Vicente Estrada-Carpenter,[57] Sandra M. Faber,[58] Vital Fernández,[33] Keely D. Finkelstein[1] and Jonathan Freundlich,[59] Seiji Fujimoto,[60,61] Ángela García-Argumánez,[62,63] Jonathan P. Gardner,[20] Eric Gawiser,[64] Carlos Gómez-Guijarro,[65] Yuchen Guo,[1] Kurt Hamblin,[25] Timothy S. Hamilton,[66] Nimish P. Hathi,[3] Benne W. Holwerda,[67] Michaela Hirschmann,[68] Taylor A. Hutchison,[13,5,6] Saurabh W. Jha,[64] Shardha Jogee,[1] Stéphanie Juneau,[69] Intae Jung,[70,20,71] Susan A. Kassin,[72,73] Aurélien Le Bail,[56] Gene C. K. Leung,[1] Ray A. Lucas,[3] Benjamin Magnelli,[51] Kameswara Bharadwaj Mantha,[74] Jasleen Matharu,[5,6] Elizabeth J. McGrath,[8] Daniel H. McIntosh,[75] Emiliano Merlin,[76] Bahram Mobasher,[77] Jeffrey A. Newman,[78] David C. Nicholls,[79] Viraj Pandya,[80,†] Marc Rafelski,[3,81] Kaila Ronayne,[5,6] Paola Santini,[21] Lise-Marie Seillé,[7] Ekta A. Shah,[82] Lu Shen,[83,84] Raymond C. Simons,[3] Gregory F. Snyder,[3] Elizabeth R. Stanway,[85] Amber N. Straughn,[20] Harry I. Teplitz,[86] Brittany N. Vanderhoof,[5,6] Jesús Vega-Ferrero,[9] Weichen Wang,[87] Benjamin J. Weiner,[88] Christopher N. A. Willmer,[89] Stijn Wuyts,[90] Jorge A. Zavala[91]

[1] Department of Astronomy, The University of Texas at Austin, Austin, TX, USA

[2] NSF's National Optical-Infrared Astronomy Research Laboratory, 950 N. Cherry Ave., Tucson, AZ 85719, USA

[3] Space Telescope Science Institute, 3700 San Martin Drive, Baltimore, MD 21218, USA

[4] Laboratory for Multiwavelength Astrophysics, School of Physics and Astronomy, Rochester Institute of Technology, 84 Lomb Memorial Drive, Rochester, NY 14623, USA

[5] Department of Physics and Astronomy, Texas A&M University, College Station, TX, 77843-4242 USA

[6] George P. and Cynthia Woods Mitchell Institute for Fundamental Physics and Astronomy, Texas A&M University, College Station, TX, 77843-4242 USA

[7] Aix Marseille Univ, CNRS, CNES, LAM Marseille, France

[8] Department of Physics and Astronomy, Colby College, Waterville, ME 04901, USA

[9] Instituto de Astrofísica de Canarias, La Laguna, Tenerife, Spain

[10] Universidad de la Laguna, La Laguna, Tenerife, Spain

[11] Université Paris-Cité, LERMA - Observatoire de Paris, PSL, Paris, France

[12] Dunlap Institute for Astronomy & Astrophysics, University of Toronto, Toronto, ON M5S 3H4, Canada

[13] NSF Graduate Fellow

[14] Centro de Astrobiología (CAB/CSIC-INTA), Ctra. de Ajalvir km 4, Torrejón de Ardoz, E-28850, Madrid, Spain

[15] Kavli Institute for Cosmology, University of Cambridge, Madingley Road, Cambridge, CB3 0HA, UK

[16] Cavendish Laboratory, University of Cambridge, 19 JJ Thomson Avenue, Cambridge, CB3 0HE, UK

[17] Astronomy Centre, University of Sussex, Falmer, Brighton BN1 9QH, UK

[18] Institute of Space Sciences and Astronomy, University of Malta, Msida MSD 2080, Malta

[19] Center for Computational Astrophysics, Flatiron Institute, 162 5th Avenue, New York, NY 10010, USA

[20] Astrophysics Science Division, NASA Goddard Space Flight Center, 8800 Greenbelt Rd, Greenbelt, MD 20771, USA

[21] INAF - Osservatorio Astronomico di Roma, via di Frascati 33, 00078 Monte Porzio Catone, Italy

[22] University of Massachusetts Amherst, 710 North Pleasant Street, Amherst, MA 01003-9305, USA

[23] INAF–Osservatorio Astronomico di Padova, Vicolo dell'Osservatorio 5, I-35122, Padova, Italy

[24] Harvard-Smithsonian Center for Astrophysics, 60 Garden Street, Cambridge, MA 02138, USA

[25] Department of Physics and Astronomy, University of Kansas, Lawrence, KS 66045, USA

[26] Observational Cosmology Laboratory, Code 665, NASA Goddard Space Flight Center, Greenbelt, MD 20771

[27] Gemini Observatory/NSF's National Optical-Infrared Astronomy Research Laboratory, 950 N. Cherry Ave., Tucson, AZ 85719, USA

[28] ESA/AURA Space Telescope Science Institute

[29] Department of Physics, 196 Auditorium Road, Unit 3046, University of Connecticut, Storrs, CT 06269, USA

[30] *Kapteyn Astronomical Institute, University of Groningen, P.O. Box 800, 9700 AV Groningen, The Netherlands*

[31] *SRON Netherlands Institute for Space Research, Postbus 800, 9700 AV Groningen, The Netherlands*

[32] *School of Physics and Astronomy, University of Nottingham, University Park, Nottingham NG7 2RD, UK*

[33] *Instituto de Investigación Multidisciplinar en Ciencia y Tecnología, Universidad de La Serena, Raul Bitrán 1305, La Serena 2204000, Chile*

[34] *Departamento de Astronomía, Universidad de La Serena, Av. Juan Cisternas 1200 Norte, La Serena 1720236, Chile*

[35] *Centro de Astrobiología (CSIC-INTA), Ctra de Ajalvir km 4, Torrejón de Ardoz, 28850, Madrid, Spain*

[36] *Department of Physics, 196 Auditorium Road, Unit 3046, University of Connecticut, Storrs, CT 06269*

[37] *Department of Physics, University of the Pacific, Stockton, CA 90340 USA*

[38] *Department of Astronomy and Steward Observatory, University of Arizona, Tucson, AZ 85721, USA*

[39] *Division of Science, National Astronomical Observatory of Japan, 2-21-1 Osawa, Mitaka, Tokyo 181-8588, Japan*

[40] *Department of Astronomy, University of Michigan, 1085 S. University Ave, Ann Arbor, MI 48109-1107, USA*

[41] *European Space Agency, ESA/ESTEC, Keplerlaan 1, 2201 AZ Noordwijk, NL*

[42] *Dipartimento di Fisica e Astronomia "G.Galilei", Universitá di Padova, Via Marzolo 8, I-35131 Padova, Italy*

[43] *Departamento de Física Teórica, Atómica y Óptica, Universidad de Valladolid, 47011 Valladolid, Spain*

[44] *Instituto de Astrofísica e Ciências do Espaço, Universidade de Lisboa, OAL, Tapada da Ajuda, PT1349-018 Lisbon, Portugal*

[45] *Osservatorio Astronomico di Roma, via Frascati 33, Monte Porzio Catone, Italy*

[46] *School of Earth and Space Exploration, Arizona State University, Tempe, AZ, 85287 USA*

[47] *AAAS S&T Policy Fellow hosted at the National Science Foundation, 1200 New York Ave, NW, Washington, DC, US 20005*

[48] *Department of Physics & Astronomy, University of California, Irvine, 4129 Reines Hall, Irvine, CA 92697, USA*

[49] *Centre for Astrophysics & Supercomputing, Swinburne University of Technology, Hawthorn, VIC 3122, Australia*

[50] *ARC Centre of Excellence for All Sky Astrophysics in 3 Dimensions (ASTRO 3D)*

[51] *Université Paris-Saclay, Université Paris Cité, CEA, CNRS, AIM, 91191, Gif-sur-Yvette, France*

[52] *Institute for Astronomy, University of Edinburgh, Blackford Hill, Edinburgh, EH9 3HJ UK*

[53] *Department of Physics and Astronomy, University of the Western Cape, Robert Sobukwe Rd, Bellville, Cape Town 7535, South Africa*

[54] *Department of Physics and Astronomy, Johns Hopkins University, Baltimore, MD, USA*

[55] *Racah Institute of Physics, The Hebrew University of Jerusalem, Jerusalem 91904, Israel*

[56] *Université Paris-Saclay, Université Paris Cité, CEA, CNRS, AIM, 91191, Gif-sur-Yvette, France*

[57] *Department of Astronomy & Physics, Saint Mary's University, 923 Robie Street, Halifax, NS, B3H 3C3, Canada*

[58] *University of California Observatories and Department of Astronomy and Astrophysics, University of California, Santa Cruz, 1156 High Street, Santa Cruz, CA 95064, USA*

[59] *Université de Strasbourg, CNRS, Observatoire Astronomique de Strasbourg, UMR 7550, F-67000 Strasbourg, France*

[60] *Cosmic Dawn Center (DAWN), Jagtvej 128, DK2200 Copenhagen N, Denmark*

[61] *Niels Bohr Institute, University of Copenhagen, Lyngbyvej 2, DK2100 Copenhagen Ø, Denmark*

[62] *Departamento de Física de la Tierra y Astrofísica, Facultad de CC Físicas, Universidad Complutense de Madrid, E-28040, Madrid, Spain*

[63] *Instituto de Física de Partículas y del Cosmos IPARCOS, Facultad de CC Físicas, Universidad Complutense de Madrid, 28040 Madrid, Spain*

[64] *Department of Physics and Astronomy, Rutgers, the State University of New Jersey, Piscataway, NJ 08854, USA*

[65] *Université Paris-Saclay, Université Paris Cité, CEA, CNRS, AIM, 91191, Gif-sur-Yvette, France*

[66] *Shawnee State University, Portsmouth, OH, USA*

[67] *Physics & Astronomy Department, University of Louisville, 40292 KY, Louisville, USA*

[68] *Institute of Physics, Laboratory of Galaxy Evolution, Ecole Polytechnique Fédérale de Lausanne (EPFL), Observatoire de Sauverny, 1290 Versoix, Switzerland*

[69] *NSF's NOIRLab, 950 N. Cherry Ave., Tucson, AZ 85719, USA*

[70] *Department of Physics, The Catholic University of America, Washington, DC 20064, USA*

[71] *Center for Research and Exploration in Space Science and Technology, NASA/GSFC, Greenbelt, MD 20771*

[72] *Space Telescope Science Institute, Baltimore, MD, 21218, USA*

[73] *Dept. of Physics & Astronomy, Johns Hopkins University, 3400 N. Charles St., Baltimore, MD, 21218, USA*

[74] *Minnesota Institute for Astrophysics, University of Minnesota, 116 church St SE, Minneapolis, MN, 55455, USA.*

[75] *Division of Energy, Matter and Systems, School of Science and Engineering, University of Missouri-Kansas City, Kansas City, MO 64110, USA*

[76] *INAF Osservatorio Astronomico di Roma, Via Frascati 33, 00078 Monteporzio Catone, Rome, Italy*

[77] *Department of Physics and Astronomy, University of California, 900 University Ave, Riverside, CA 92521, USA*

[78] *Department of Physics and Astronomy and PITT PACC, University of Pittsburgh, Pittsburgh, PA 15260, USA*

[79] *Research School of Astronomy and Astrophysics, Australian National University, Canberra, ACT 2600, Australia*

[80] *Columbia Astrophysics Laboratory, Columbia University, 550 West 120th Street, New York, NY 10027, USA*

[81] *Department of Physics and Astronomy, Johns Hopkins University, Baltimore, MD 21218, USA*

[82] *Department of Physics and Astronomy, University of California,Davis, One Shields Ave, Davis, CA 95616, USA*

[83] *CAS Key Laboratory for Research in Galaxies and Cosmology, Department of Astronomy, University of Science and Technology of China, Hefei 230026, China*

[84] *School of Astronomy and Space Sciences, University of Science and Technology of China, Hefei, 230026, China*

[85] *Department of Physics, University of Warwick, Coventry, CV4 7AL, United Kingdom*

[86] *IPAC, Mail Code 314-6, California Institute of Technology, 1200 E. California Blvd., Pasadena CA, 91125, USA*

[87] *Department of Physics and Astronomy, Johns Hopkins University, 3400 N. Charles Street, Baltimore, MD 21218, USA*

[88] *MMT/Steward Observatory, University of Arizona, 933 N. Cherry St, Tucson, AZ 85721, USA*

[89] *Steward Observatory, University of Arizona, 933 N. Cherry Ave, Tucson, AZ 85721,USA*

[90] *Department of Physics, University of Bath, Claverton Down, Bath BA2 7AY, UK*

[91] *National Astronomical Observatory of Japan, 2-21-1 Osawa, Mitaka, Tokyo 181-8588, Japan*